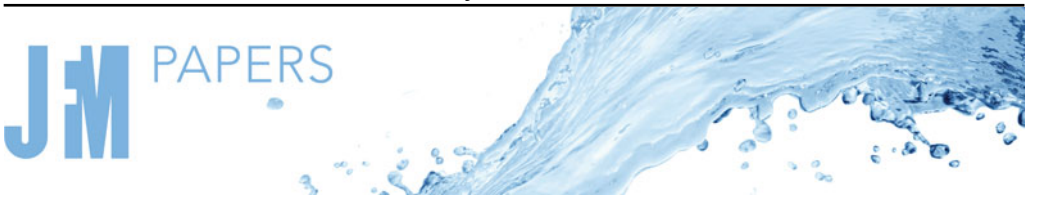
J. Fluid Mech. (2026), *vol.* 1030, A37, doi:10.1017/jfm.2026.11235



Non-uniformities in miscible surfactant-laden two-layer thin liquid films

Rayan Barry[1] **and Satish Kumar**[1]

[1]Department of Chemical Engineering and Materials Science, University of Minnesota, Minneapolis, MN 55455, USA

Corresponding author: Satish Kumar, kumar030@umn.edu

(Received 19 October 2025; revised 18 January 2026; accepted 22 January 2026)

Thin liquid films play an instrumental role in the coating industry. In many cases, these films consist of multiple components and are applied in multiple layers. However, multilayer multicomponent coatings can readily develop thickness non-uniformities due to Marangoni flows driven by solute concentration gradients. Previous flow visualisation experiments have demonstrated that the addition of surfactant can suppress such non-uniformities, but the physical mechanisms underlying this suppression have not yet been definitively established. We investigate the growth of film-height non-uniformities in a two-layer multicomponent coating consisting of a solute-rich bottom layer, a solute-depleted top layer and surfactant. A lubrication-theory-based model that accounts for vertical and lateral gradients in solute and surfactant concentrations is developed. The resulting coupled nonlinear partial differential equations describing the film height, solute concentration and surfactant concentration are solved with a pseudospectral method. Our findings reveal that surfactant-induced Marangoni flows can significantly decrease film-height non-uniformities by competing with Marangoni flows due to solute concentration gradients. Several simplifications of the governing equations are explored to determine how well predictions from these simplified models compare with the full lubrication-theory-based model, thereby providing insight into dominant physical mechanisms in different parameter regimes. The role of surfactant solubility and sorption kinetics in controlling perturbation growth is also examined.

Key words: interfacial flows (free surface), thin films

1. Introduction

Thin liquid films appear in the fabrication processes of a wide range of technologically important products such as fuel cells (Will *et al.* 2000), organic light-emitting diode

© The Author(s), 2026. Published by Cambridge University Press. This is an Open Access article, distributed under the terms of the Creative Commons Attribution licence (https://creativecommons.org/licenses/by/4.0/), which permits unrestricted re-use, distribution and reproduction, provided the original article is properly cited.

https://doi.org/10.1017/jfm.2026.11235 Published online by Cambridge University Press

screens (Eccher *et al.* 2015), perovskite photovoltaics (Todorov & Mitzi 2010) and printed electronics (Kalpathy *et al.* 2012). Carefully engineered solution mixtures are often deposited as liquid layers and solidified via evaporation, curing, or other methods to produce coatings with unique features and properties. In the case of photovoltaics, anti-reflection coatings reduce the glare of solar cells (Iwe *et al.* 2019), solution-based perovskite coatings increase power conversion efficiencies (Park & Zhu 2020) and polymer layers provide optical enhancement (Ng *et al.* 2007). The desired functionalities are frequently obtained by applying multiple layers in tandem, each unique in composition and exhibiting important properties.

Two of the essential requirements to avoid degraded product performance and achieve the intended coating properties are a uniform film thickness and well-controlled concentration distributions. However, minor perturbations arising from contaminants, substrate defects, flow rate oscillations or other sources may lead to variations in the film height and concentration distributions. Solute concentration gradients at the interface can develop over time, produce surface-tension gradients and induce a Marangoni flow. These flows can deform the interface, causing undesired film-height non-uniformities that may lead to film rupture and dewetting. While variations in film height also generate capillary flows that counteract interface deformation and level the film, subsequent drying and solidification may lock in film-height non-uniformities before significant levelling occurs.

One strategy to minimise film-height non-uniformities is to add surfactants. Horiuchi, Suszynski & Carvalho (2015) experimentally observed dewetting in miscible two-layer films with a vertically stratified solute concentration. Through two-layer slot coating, they applied an ethanol-rich bottom layer and a water-rich top layer of glycerol-based solutions onto a moving substrate. (It should be noted that the two-layer structure is most distinct at early times. As time progresses, solute diffusion causes the solute concentration to become more homogeneous.) Different concentrations of the surfactant sodium dodecyl sulphate (SDS) were added to the top layer and the coating was visualised downstream for various liquid viscosities, surface tensions and film-thickness ratios. If the surfactant concentration was too low, significant dewetting of the coating was observed. However, at a critical surfactant concentration, a uniform film thickness was recovered. It was hypothesised that uneven ethanol diffusion from the bottom layer to the liquid–air interface led to Marangoni stresses that deformed the interface to such an extent that dewetting occurred, but the physical mechanisms underlying the stabilising influence of surfactants in such multilayer multicomponent miscible coatings remain unclear. In particular, Horiuchi *et al.*, did not address the possibility that Marangoni stresses due to surfactant concentration gradients could counteract Marangoni stresses due to solute concentration gradients.

Motivated by the experiments of Horiuchi *et al.*, Larsson & Kumar (2021) investigated the evolution of non-uniformities in non-volatile miscible two-layer films devoid of surfactants using a lubrication-theory-based model that accounts for vertical stratification of the solute concentration. It was found that uneven solute diffusion from the bottom layer, driven by an initial lateral perturbation imposed on the solute concentration, can generate significant height perturbations via solute Marangoni stresses. This is especially pronounced when solute convection is sufficiently strong relative to solute diffusion, leading to circulatory convective patterns and intensifying the deformation of the interface. However, their model did not include surfactants, which could potentially have a significant influence on film-height non-uniformities and composition gradients within the film. Surfactant effects on the surface tension are coupled to solute Marangoni stresses in non-trivial ways, making *a priori* predictions difficult. To the best of our knowledge, a theoretical investigation of combined solute and surfactant effects in such miscible multilayer films has yet to be reported.

https://doi.org/10.1017/jfm.2026.11235 Published online by Cambridge University Press

Many previous studies have employed a rapid-vertical-diffusion approximation to model multicomponent thin films (Jensen & Grotberg 1993; Eres, Weidner & Schwartz 1999; Pham, Cheng & Kumar 2017; Pham & Kumar 2019; Larsson & Kumar 2021, 2022; Moore, Vella & Oliver 2021). These models assume that the time scale for vertical diffusion is sufficiently rapid relative to other phenomena such as convection, and give rise to a uniform species distribution in the vertical direction. However, such simplifications fail to consider the influence of severe composition disparities between individual layers, which often exist in multilayer structures (Schulz & Keddie 2018), and neglect vertical concentration gradients that develop due to evaporation (Larsson & Kumar 2022). Slow vertical diffusion of the solute due to a non-homogeneous vertical concentration profile can severely impact film behaviour in such cases and play a significant role in the onset and growth of height perturbations (Larsson & Kumar 2021). As a result, the rapid-vertical-diffusion approximation is not useful for examining two-layer structures where a severe disparity in the composition of the layers exists (Köllner *et al.* 2013), such as the stratified system investigated by Horiuchi *et al.* (2015). Although some recent work on the uniformity of thin liquid films retained the vertical stratification of solute (Serpetsi & Yiantsios 2012; Yiantsios *et al.* 2015; Dey *et al.* 2019; Rodríguez-Hakim *et al.* 2019; Larsson & Kumar 2021; Chen, Driscoll & Braun 2024), the extent to which surfactants can stabilise multilayer multicomponent coatings where large vertical gradients may exist, and where solute and surfactant effects may be coupled, remains an open question.

In the present work, we extend the model of Larsson & Kumar (2021) by taking into account surfactant Marangoni effects. In § 2, we formulate the mathematical model. In § 3, we develop simplified models to gain additional insight into underlying physical mechanisms. In § 4, surfactants are introduced as an insoluble component localised to the liquid–air interface and in § 5 as a soluble component concentrated in the top layer. We present parametric studies to isolate regimes with qualitatively different film behaviour and identify the physical mechanisms through which surfactants stabilise multilayer coatings and help recover a uniform film thickness. We also qualitatively compare our model's predictions with the experimental findings of Horiuchi *et al.* (2015). Conclusions are given in § 6.

2. Mathematical model

We consider a liquid film consisting of non-volatile solvent, solute and soluble surfactant in Cartesian coordinates (x^*, z^*) resting on a solid substrate at $z^* = 0$, as shown in figure 1. Here, x^* corresponds to the horizontal direction, z^* denotes the vertical direction and t^* is time. In this work, * superscripts denote dimensional variables that will later be non-dimensionalised. The film comprises two miscible Newtonian liquid layers: a solute-depleted top layer and a solute-rich bottom layer. The film height $h^*(x^*, t^*)$, solute concentration $\phi^*(x^*, z^*, t^*)$, interface surfactant concentration $\Gamma^*(x^*, t^*)$ and bulk surfactant concentration $c^*(x^*, z^*, t^*)$ are the variables of interest. We impose periodic conditions in x^* and assume constant viscosity μ, liquid density ρ, solute diffusivity D, surface surfactant diffusivity D_s and bulk surfactant diffusivity D_b. We also assume dilute solute and surfactant concentrations and neglect evaporation to identify the basic mechanisms through which surfactants influence film-height non-uniformities.

2.1. *Hydrodynamics*

We assume that the film is thin enough so that gravitational forces are negligible but thick enough so that disjoining pressure arising from van der Waals interactions can be neglected. The balance of viscous and surface-tension stresses provides a characteristic

https://doi.org/10.1017/jfm.2026.11235 Published online by Cambridge University Press

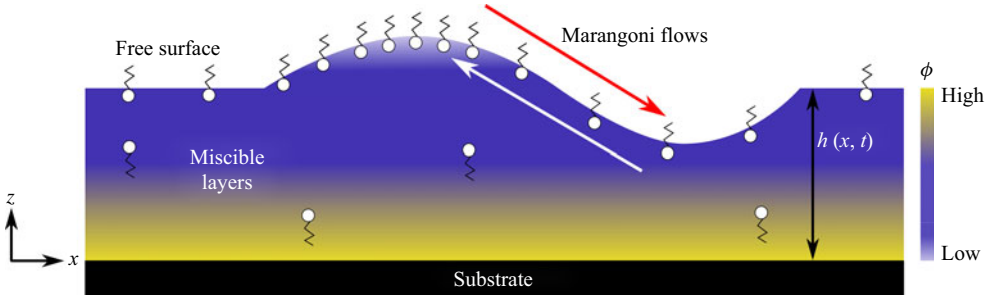


Figure 1. Schematic representation of a two-layer liquid film resting on a solid substrate. The film comprises solvent, solute and soluble surfactant. Yellow indicates a higher solute concentration. Perturbations to the solute and surfactant concentration profiles at the interface can produce Marangoni flows. The convex region shown is surfactant-rich and solute-depleted relative to the concave region. The resulting surface-tension gradients can produce solute and surfactant Marangoni flows depicted by the solid white and red arrows, respectively.

horizontal velocity scale $U = \sigma_0 H^3/\mu L^3$, where H is the initial mean film thickness, L is a characteristic horizontal length scale and σ_0 is the solvent surface tension. The characteristic horizontal length scale L can be obtained from a balance of viscous and solute Marangoni stresses

$$\frac{\mu U}{H} \sim \frac{w_{solute}\Delta\sigma}{L} \Rightarrow L \sim \frac{H}{\sqrt{Ma}}. \tag{2.1}$$

Here, w_{solute} is the initial solute mass fraction and $\Delta\sigma = \sigma_0 - \sigma_{solute}$ is the difference between the solvent and solute surface tensions. The solute Marangoni number $Ma = (w_{solute}\Delta\sigma)/\sigma_0$ provides a measure of the strength of solute-induced surface-tension gradients relative to the solvent surface tension.

We assume that the ratio between the vertical and horizontal characteristic lengths $\epsilon = H/L \ll 1$, allowing the use of the lubrication approximation (Oron, Davis & Bankoff 1997). We non-dimensionalise variables using the following scalings:

$$x^* = xL,\ z^* = z\epsilon L,\ h^* = h\epsilon L,\ \sigma^* = \sigma\sigma_0,\ u^* = u\frac{\sigma_0\epsilon^3}{\mu},$$
$$w^* = w\epsilon\frac{\sigma_0\epsilon^3}{\mu},\ t^* = t\frac{L\mu}{\sigma_0\epsilon^3},\ p^* = p\frac{\sigma_0\epsilon}{L},\ \phi^* = \phi\,\phi_0,\ \Gamma^* = \Gamma\,\Gamma_0, \tag{2.2}$$

where (u^*, w^*) is the velocity and p^* is the pressure. The solute concentration ϕ^* is scaled by an initial concentration ϕ_0, the interface surfactant concentration Γ^* is scaled by the initial surface surfactant concentration Γ_0 and the pressure p^* is scaled by a capillary pressure obtained from the normal stress balance at the interface. The kinematic condition gives the scale L/U for time. Note that $Ma = \epsilon^2$ due to the choice of lateral length scale in (2.1).

The lubrication approximation of the Navier–Stokes equations in two dimensions leads to a nonlinear evolution equation for $h(x, t)$

$$\frac{\partial h}{\partial t} = -\frac{\partial}{\partial x}\left[\frac{\partial^3 h}{\partial x^3}\frac{h^3}{3}\right] - \frac{\partial}{\partial x}\left[\frac{h^2}{2}\left(\frac{1}{Ma}\frac{\partial\sigma}{\partial x}\right)\right]. \tag{2.3}$$

https://doi.org/10.1017/jfm.2026.11235 Published online by Cambridge University Press

Here, $\sigma(x,t)$ is the surface tension of the liquid. The velocity field is given by

$$u = -\frac{\partial^3 h}{\partial x^3}\frac{z^2}{2} + \left(\frac{1}{\epsilon^2}\frac{\partial \sigma}{\partial x} + \frac{\partial^3 h}{\partial x^3}h\right) z, \tag{2.4}$$

$$w = \frac{\partial^4 h}{\partial x^4}\frac{z^3}{6} - \left[\frac{1}{\epsilon^2}\frac{\partial^2 \sigma}{\partial x^2} + \frac{\partial}{\partial x}\left(\frac{\partial^3 h}{\partial x^3}h\right)\right]\frac{z^2}{2}. \tag{2.5}$$

A detailed derivation of (2.3), (2.4) and (2.5) is provided in § S.1 of the supplementary material.

When surfactants are absent and the solute is sufficiently dilute, the surface-tension equation of state is linear in the solute concentration (Serpetsi & Yiantsios 2012; Köllner *et al.* 2013; Larsson & Kumar 2021)

$$\sigma^* = \sigma_0 - \left(\frac{\partial \sigma^*}{\partial \phi^*}\right)\Big|_{\phi^*=0} \phi^*|_{z=h}. \tag{2.6}$$

In non-dimensional form, (2.6) becomes

$$\sigma = 1 - Ma\,\phi|_{z=h}. \tag{2.7}$$

In the experiments of Horiuchi *et al.* (2015), ethanol was the solute of interest. For ethanol mass fractions $w_{solute} < 0.1$, a linear dependence of the surface tension on ϕ was previously found to be reasonably accurate (Vazquez, Alvarez & Navaza 1995) and is the simplest relationship for this dependence to probe physical mechanisms. We take $Ma > 0$ because most alcohols are weakly surface active and lower the surface tension of the liquid (Kahlweit, Strey & Busse 1991; Horiuchi *et al.* 2015), and this was the case studied by Larsson and Kumar in the absence of surfactants (Larsson & Kumar 2021). The case $Ma < 0$ can occur in practice, for instance in the case of salts (Benouaguef *et al.* 2021) and acrylic resins (Wilson 1993), but is not explored in this work.

When surfactants are present in dilute concentrations, the surface tension can be written as a linear function of both the solute and surfactant concentrations (Pham & Kumar 2019)

$$\sigma = 1 - Ma\,\phi|_{z=h} - Ma_s\,\Gamma. \tag{2.8}$$

Here, $Ma_s = (w_{surfactant}\Delta\sigma_s)/\sigma_0$ is a surfactant Marangoni number defined with respect to the surfactant mass fraction $w_{surfactant}$ and the solvent–surfactant surface-tension difference $\Delta\sigma_s = \sigma_0 - \sigma_{surfactant}$.

Inserting (2.8) into (2.3) yields

$$\frac{\partial h}{\partial t} = -\underbrace{\frac{\partial}{\partial x}\left[\frac{\partial^3 h}{\partial x^3}\frac{h^3}{3}\right]}_{\text{capillary levelling}} + \underbrace{\frac{\partial}{\partial x}\left[\frac{h^2}{2}\frac{\partial \phi|_{z=h}}{\partial x}\right]}_{\text{solute Marangoni flow}} + \underbrace{\frac{\partial}{\partial x}\left[\frac{Ma_s}{Ma}\frac{h^2}{2}\frac{\partial \Gamma}{\partial x}\right]}_{\text{surfactant Marangoni flow}}. \tag{2.9}$$

The first term on the right-hand side describes a contribution due to pressure-driven flows produced by interface curvature, or capillary levelling. The second and third terms, respectively, contain contributions of surface-tension gradients arising from spatial variations of solute and surfactant concentrations at the interface.

2.2. *Solute transport*

The transport of solute is governed by the convection–diffusion equation

$$\frac{\partial \phi}{\partial t} + u\frac{\partial \phi}{\partial x} + w\frac{\partial \phi}{\partial z} = \frac{1}{Pe}\frac{\partial^2 \phi}{\partial x^2} + \frac{1}{Pe\,\epsilon^2}\frac{\partial^2 \phi}{\partial z^2}. \tag{2.10}$$

https://doi.org/10.1017/jfm.2026.11235 Published online by Cambridge University Press

Here, $Pe = LU/D$ is the solute Péclet number, which gives a ratio of horizontal diffusive and convective time scales. Equation (2.10) is subject to no-flux boundary conditions at the substrate and a mass-conservation condition at the liquid–air interface

$$\left.\frac{\partial \phi}{\partial z}\right|_{z=0} = 0, \tag{2.11}$$

$$\left.\frac{\partial \phi}{\partial z}\right|_{z=h} - \epsilon^2 \frac{\partial h}{\partial x}\left.\frac{\partial \phi}{\partial x}\right|_{z=h} = 0. \tag{2.12}$$

We note that the lubrication approximation has not been invoked in (2.10) and (2.12) in order to retain vertical solute concentration gradients, which are expected to play a key role in vertically stratified multilayer systems (Larsson & Kumar 2021).

2.3. *Insoluble surfactant*

The surfactant is assumed to be insoluble in § 4 and its transport is governed in the lubrication limit by (Pereira & Kalliadasis 2008)

$$\frac{\partial \Gamma}{\partial t} + \frac{\partial \left(u|_{z=h}\Gamma\right)}{\partial x} = \frac{1}{Pe_s}\frac{\partial^2 \Gamma}{\partial x^2}, \tag{2.13}$$

where $Pe_s = LU/D_s$ is the surfactant Péclet number at the interface. The first term of (2.13) describes the evolution of surfactant concentration with time, the second term describes convective transport of surfactant at the interface and the last term accounts for surfactant diffusion along the interface.

2.4. *Soluble surfactant*

We assume in this work that equilibrium relationships between the surface tension and species concentration hold at all times, and thus the surface tension at a given time σ is the surface tension σ_{eq} achieved under equilibrium conditions with respect to the surface concentration Γ. It is also assumed that the surfactant concentration is sufficiently dilute so that micelles do not form.

For dilute surfactant concentrations, a Henry's law isotherm relates surfactant concentration in the bulk and at the interface (Prosser & Franses 2001)

$$\Gamma^* = K_H c^*|_{z=h}. \tag{2.14}$$

The surfactant's efficiency of adsorption is described by K_H, an equilibrium constant measuring the surface activity of a given surfactant in a solvent of interest. A flux J^* describing deviation from equilibrium is obtained using the relation

$$J^* = k^H_{ads} c^*|_{z=h} - k^H_{des}\Gamma^*, \tag{2.15}$$

where k^H_{ads} and k^H_{des} are first-order rate constants of adsorption and desorption, respectively. We note that $K_H = k^H_{ads}/k^H_{des}$, consistent with the equilibrium condition $J^* = 0$.

We assume equilibrium at $t = 0$ between the surfactant-laden liquid layer and the interface. The scale for the bulk concentration is determined by

$$c^* = c\, c_{s,0} \text{ with } c_{s,0} = \frac{k^H_{des}\Gamma_0}{k^H_{ads}}, \tag{2.16}$$

where $c_{s,0}$ denotes the initial subsurface surfactant concentration in the bulk (i.e. at $t = 0$ and at $z = h$). This scale assumes fast surfactant-exchange kinetics between the bulk and

https://doi.org/10.1017/jfm.2026.11235 Published online by Cambridge University Press

the interface relative to surfactant diffusion in the bulk, and an initially uniform surfactant concentration $c_{s,0}$ at the subsurface in equilibrium with surfactant at the interface.

With this scaling, the dimensionless form of (2.15) is

$$J = Bi\ (c|_{z=h} - \Gamma)\,, \tag{2.17}$$

where $Bi = k^H_{des} L/U$ acts as a Biot number and provides a ratio between the time scale of the flow and the time scale of desorption.

Surfactant interface transport is governed by the equation

$$\frac{\partial \Gamma}{\partial t} + \frac{\partial\ (u|_{z=h}\Gamma)}{\partial x} = \frac{1}{Pe_s}\frac{\partial^2 \Gamma}{\partial x^2} + J, \tag{2.18}$$

where the added term J, given by (2.17), accounts for the exchange flux due to adsorption–desorption kinetics. Note that (2.13) is recovered when $J = 0$. The bulk surfactant concentration $c(x, z, t)$ is governed by the convection–diffusion equation

$$\frac{\partial c}{\partial t} + u\frac{\partial c}{\partial x} + w\frac{\partial c}{\partial z} = \frac{1}{Pe_b}\frac{\partial^2 c}{\partial x^2} + \frac{1}{Pe_b\,\epsilon^2}\frac{\partial^2 c}{\partial z^2}, \tag{2.19}$$

where $Pe_b = LU/D_b$ is the bulk surfactant Péclet number. The lubrication approximation was not invoked here in order to retain the effects of vertical surfactant concentration gradients in the bulk.

Boundary conditions enforce no flux at the substrate and a balance at the interface relating the diffusive flux of surfactant from the bulk to the interface through J

$$\left.\frac{\partial c}{\partial z}\right|_{z=0} = 0, \tag{2.20}$$

$$\left.\frac{\partial c}{\partial z}\right|_{z=h} - \epsilon^2 \frac{\partial h}{\partial x}\left.\frac{\partial c}{\partial x}\right|_{z=h} = -\epsilon^2 Pe_b Bi\beta\ (c|_{z=h} - \Gamma)\,. \tag{2.21}$$

Here, (2.21) is determined from Fick's law with $J = D_b\ \boldsymbol{n}\cdot\nabla c|_{z=h}$ (Kalogirou & Blyth 2020), where $\boldsymbol{n} = (-\partial h/\partial x, 1)$ defines the outward unit vector normal to the interface under the lubrication approximation. The parameter $\beta = k^H_{ads}/(k^H_{des}H)$ is a solubility coefficient describing the strength of adsorption relative to desorption. Larger β values correspond to less soluble surfactants, with the surfactant behaving as insoluble for $\beta \gg 1$.

The insoluble-surfactant case is described by (2.9), (2.10) and (2.13), while the soluble-surfactant case is described by (2.9), (2.10), (2.18) and (2.19). Note that (2.9) and (2.13) are equivalent to some of the equations derived in Edmonstone, Craster & Matar (2006) when the capillary velocity scale is chosen (i.e. $Ca = 1$, where Ca is the capillary number). Typical values for variables and parameters are presented in tables 1 and 2.

2.5. *Initial conditions*

Motivated by prior work (Larsson & Kumar 2021), we approximate the initial condition of the two-layer coating (figure 1) through two transition functions T_{solute} and $T_{surfactant}$, achieving the desired stratification between the component-rich and component-depleted layers

https://doi.org/10.1017/jfm.2026.11235 Published online by Cambridge University Press

Parameter	Definition	Typical values
H (m)	Film thickness	$10^{-5} - 10^{-4}$ (Horiuchi *et al.* 2015)
L (m)	Characteristic horizontal length	$10^{-4} - 10^{-3}$ (Horiuchi *et al.* 2015)
μ (Pa s)	Solvent viscosity	$10^{-4} - 10^{-3}$ (Larsson & Kumar 2021)
σ_0 (N m^{-1})	Solvent surface tension	$10^{-2} - 10^{-1}$ (Horiuchi *et al.* 2015)
$\Delta\sigma$ (N m^{-1})	Solvent–solute surface-tension difference	$10^{-2} - 10^{-1}$ (Alkindi *et al.* 2008; Horiuchi *et al.* 2015)
$\Delta\sigma_s$ (N m^{-1})	Solvent–surfactant surface-tension difference	$10^{-2} - 10^{-1}$ (Woolfrey *et al.* 1986; Horiuchi *et al.* 2015)
D (m^2 s^{-1})	Solute diffusivity	10^{-9} (Pratt & Wakeham 1974)
D_b (m^2 s^{-1})	Surfactant bulk diffusivity	$10^{-11} - 10^{-9}$ (Weinheimer *et al.* 1981; Matar 2002; Barhoum & Yethiraj 2010; Morgan *et al.* 2012; Samanta 2025)
D_s(m^2 s^{-1})	Surfactant surface diffusivity	$10^{-12} - 10^{-10}$ (Henderson & Micale 1993; Phan *et al.* 2005; Samanta 2025)
w_{solute}	Solute mass fraction	$10^{-2} - 10^{-1}$ (Horiuchi *et al.* 2015)
$w_{surfactant}$	Surfactant mass fraction	$10^{-4} - 10^{-1}$ (Horiuchi *et al.* 2015)
k^H_{ads} (m s^{-1})	Linear adsorption rate	$10^{-6} - 10^{-3}$ (Chang & Franses 1995)
k^H_{des} (s^{-1})	Linear desorption rate	$10^{-2} - 10^{2}$ (Chang & Franses 1995)

Table 1. Order-of-magnitude estimates of important dimensional parameters.

Parameter	Definition	Typical values
$\epsilon = H/L$	Vertical length/Lateral length	$10^{-2} - 10^{-1}$
$Ma = w_{solute}\Delta\sigma/\sigma_0$	Solute Marangoni number	$10^{-4} - 10^{-2}$
$Ma_s = w_{surfactant}\Delta\sigma_s/\sigma_0$	Surfactant Marangoni number	$0 - 10^{-1}$
$Pe = H\sigma_0\epsilon^2/D\mu$	Solute Péclet number	$10^2 - 10^6$
$Pe_s = H\sigma_0\epsilon^2/D_s\mu$	Surfactant surface Péclet number	$10^3 - 10^6$
$Pe_b = H\sigma_0\epsilon^2/D_b\mu$	Surfactant bulk Péclet number	$10^2 - 10^6$
$Bi = k^H_{des}L\mu/\epsilon^3\sigma_0$	Biot number	$10^{-3} - 10^3$
$\beta = k^H_{ads}/k^H_{des}H$	Solubility coefficient	$10^{-3} - 10^3$

Table 2. Typical range of dimensionless parameters explored in this work using the dimensional parameter values from table 1 .

$$T_{solute}(z;\, h_b,\, s) = \begin{cases} 1, & \text{if } w \leqslant 0 \\ \frac{\exp(-1/(1-w))}{\exp(-1/(1-w))+\exp(-1/w)}, & \text{if } 0 < w < 1 \ \text{ where } w = \frac{z-(h_b-1/s)}{2/s}, \\ 0, & \text{if } 1 \leqslant w \end{cases} \tag{2.22}$$

$$T_{surfactant}(z;\, h_b,\, s) = \begin{cases} 0, & \text{if } w \leqslant 0 \\ 1 - \frac{\exp(-1/(1-w))}{\exp(-1/(1-w))+\exp(-1/w)}, & \text{if } 0 < w < 1 \ \text{ where } w = \frac{z-(h_b-1/s)}{2/s}. \\ 1, & \text{if } 1 \leqslant w \end{cases} \tag{2.23}$$

Here, s is the slope of the transition between layers of distinct composition and h_b is the dimensionless bottom-layer thickness. We take $s = 3$ and $h_b = 0.5$ to match previously chosen values for the surfactant-free case (Larsson & Kumar 2021). The stratification

https://doi.org/10.1017/jfm.2026.11235 Published online by Cambridge University Press

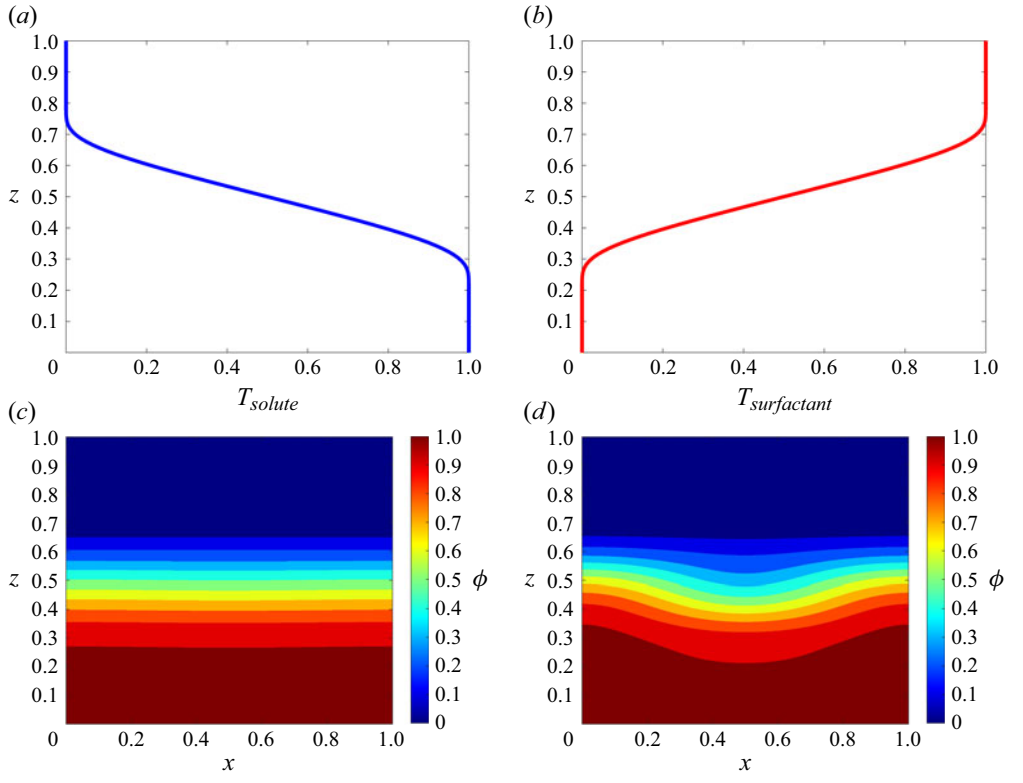


Figure 2. Transition functions for the (*a*) solute and (*b*) surfactant approximating each component's vertical stratification. The solute concentration field at $t = 0$ is shown in (*c*), and its perturbation amplitude is amplified in (*d*) from $\phi_p = 0.01$ to $\phi_p = 0.3$ so it can be seen more easily. The x-coordinate is rescaled from $[0, 2\pi/\alpha]$ to $[0, 1]$.

of solute and surfactant respectively achieved by (2.22) and (2.23) can be visualised in figures 2(*a*) and 2(*b*).

The solute transition function (2.22) models a film with a solute-depleted top layer and a solute-rich bottom layer. Consistent with prior work (Larsson & Kumar 2021), we refer to this as a two-layer film even though solute diffusion homogenises the two-layer structure as time progresses. In the absence of a lateral perturbation, diffusion would occur evenly across the film height. To better understand the onset and growth of non-uniformities driven by solute Marangoni stresses, we follow prior work (Larsson & Kumar 2021) and introduce a lateral perturbation in the solute concentration localised at $z = h_b$

$$\phi(x, z, t = 0) = T_{solute}\left[1 + \phi_p \cos(\alpha x) \exp\left(-\frac{(z - h_b)^2}{2\nu^2}\right)\right]. \tag{2.24}$$

Here, $\phi_p = 0.01$ is the perturbation amplitude (assumed small), $\alpha = 0.3$ is its wavenumber and $\nu = 0.1$ is the standard deviation of the Gaussian localising the initial perturbation at a height h_b from the substrate. This perturbation satisfies the periodic boundary conditions and corresponds to a depletion of solute at the centre of the film localised at the diffuse region between the two layers. Its localisation at $z = h_b$ allows us to more easily probe the influence of solute vertical diffusion on the system's response to the lateral disturbance, which is shown in figures 2(*c*) and 2(*d*).

https://doi.org/10.1017/jfm.2026.11235 Published online by Cambridge University Press

Initially, the fluid is at rest, the film is flat and the height is subject to the initial condition $h(x, t = 0) = 1$. Surfactant in the insoluble case is uniformly deposited as a monolayer such that $\Gamma(x, t = 0) = 1$. To qualitatively compare our model with the experiments of Horiuchi *et al.* (2015), we also investigated a configuration which involves soluble surfactant through the initial conditions $\Gamma(x, t = 0) = 1$ and $c(x, z, t = 0) = T_{surfactant}$. This corresponds to a surfactant-depleted bottom layer, a surfactant-rich top layer and equilibrium conditions at $t = 0$ between the surfactant-rich top layer and the liquid–air interface.

2.6. *Numerical method*

We implement a coordinate transformation to numerically handle the moving-boundary problem by mapping $(x, z, t) \to (\chi, \eta, \tau)$, where

$$\frac{\partial \chi}{\partial x} = 1, \quad \eta = \frac{z}{h}, \quad \frac{\partial \tau}{\partial t} = 1. \tag{2.25}$$

Scaling the z-coordinate using the height leads to a fixed-coordinate domain where the interface remains at $\eta = 1$. Further details are given in § S.2 of supplementary material. The transformed system of equations is solved on the $[0, 2\pi/\alpha] \times [0, 1]$ domain via a pseudospectral method (Trefethen 1996). Periodicity in χ warrants the use of Fourier modes for the χ domain, while a finite η domain on $[0, 1]$ warrants the use of Chebyshev polynomials for that domain (Boyd 2001). Mesh independence was achieved for the examined conditions using 50 Fourier modes or less and 150 Chebyshev polynomials or less. We used ode15s for time integration, a variable-step, variable-order implicit solver built into MATLAB. Results were validated through comparisons with prior work in the absence of surfactants (Larsson & Kumar 2021).

3. Simplified models

We develop two approximations to gain additional insight into the physical mechanisms underlying the evolution of height perturbations. We present these simplified models here, and in § 4 compare their predictions with numerical simulations (§ 2.6).

3.1. *Vertical-averaging approximation*

When $\epsilon^2 Pe \ll 1$, vertical diffusion of the solute is rapid relative to convection. Vertical solute concentration gradients are averaged out on a much faster time scale compared with the time needed to achieve maximum deformation of the film. We employ a vertical-averaging approximation (VAA) exploiting this time-scale disparity through an asymptotic expansion in powers of $\epsilon^2 Pe$

$$\phi = \phi_b(x, z, t) + \epsilon^2 Pe\, \phi_p(x, z, t) + \mathcal{O}\left[\left(\epsilon^2 Pe\right)^2\right]. \tag{3.1}$$

After substituting (3.1) into the solute convection–diffusion equation, (2.10), and employing boundary conditions (2.11) and (2.12), we recognise that ϕ_b is independent of z and obtain the governing equation

$$\frac{\partial \phi_b}{\partial t} + \overline{u}\frac{\partial \phi_b}{\partial x} = \frac{1}{h\, Pe}\frac{\partial}{\partial x}\left(h\frac{\partial \phi_b}{\partial x}\right), \tag{3.2}$$

where

$$\overline{u} = \frac{1}{h}\int_0^h u \mathrm{d}z = \frac{1}{3}h^2\frac{\partial^3 h}{\partial x^3} - \frac{1}{2}h\left(\frac{\partial \phi_b}{\partial x} + \frac{Ma_s}{Ma}\frac{\partial \Gamma}{\partial x}\right). \tag{3.3}$$

https://doi.org/10.1017/jfm.2026.11235 Published online by Cambridge University Press

A detailed derivation is provided in § S.3 of supplementary material. Equations (2.9), (3.2) and (2.13) are solved using a one-dimensional version of the numerical method described in § 2.6 which employs a Fourier expansion of $\phi_b(x,t)$, $h(x,t)$ and $\Gamma(x,t)$ for spatial discretisation and ode15s for time stepping. The solution is presented under the 'VAA' label in subsequent figures.

3.2. *Linearised theory*

When $\epsilon^2 Pe \ll 1$, vertical solute diffusion rapidly homogenises any initial vertical solute concentration gradients. By vertically averaging initial condition (2.24), we obtain

$$\phi(x, t=0) = \int_0^1 \phi(x,z,t)\mathrm{d}z = 0.5 + \overline{\phi_p}\,\cos(\alpha x), \tag{3.4}$$

where

$$\overline{\phi_p} = \phi_p \int_0^1 T_{solute} \exp\left[-\frac{(z-h_b)^2}{2\nu^2}\right]\mathrm{d}z \approx 0.00125 \ll 1. \tag{3.5}$$

When solute diffusion is sufficiently fast, convection can be neglected relative to lateral diffusion, reducing (2.10) to the diffusion equation

$$\frac{\partial \phi}{\partial t} = \frac{1}{Pe}\frac{\partial^2 \phi}{\partial x^2}, \tag{3.6}$$

where we have retained the transient term in the limit $Pe \to 0$ by rescaling time using a diffusive time scale. Equation (3.6) is subject to the vertically averaged initial condition (3.4).

We use separation of variables to look for a solution of the form $\phi(x,t) = X(x)T(t)$. Periodic boundary conditions in the lateral direction x suggest a cosine-series expansion for the solute concentration

$$\phi(x,t) = \sum_{n=0}^{\infty} a_n \exp\left(-\frac{n^2\alpha^2 t}{Pe}\right)\cos(n\alpha x). \tag{3.7}$$

Initial condition (3.4) imposes $a_0 = 0.5$ and $a_1 = \overline{\phi_p}$. Since higher-order terms decay exponentially fast, we substitute the leading-order solution $\phi(x,t) = 0.5 + \overline{\phi_p}\cos(\alpha x)\exp(-\alpha^2 t/Pe)$ into (2.9) and (2.13).

Since $\overline{\phi_p} \ll 1$, the remaining variables are expanded in powers of $\overline{\phi_p}$ as

$$h = 1 + g(t)\overline{\phi_p}\cos(\alpha x) + \mathcal{O}[(\overline{\phi_p})^2], \tag{3.8}$$

$$\Gamma = 1 + q(t)\overline{\phi_p}\cos(\alpha x) + \mathcal{O}[(\overline{\phi_p})^2]. \tag{3.9}$$

This expansion represents an initially uniform film thickness and surfactant concentration field with a small lateral perturbation.

Inserting (3.8) and (3.9) into (2.9) and (2.13) yields the $\mathcal{O}[\overline{\phi_p}]$ problem

$$\frac{\mathrm{d}g(t)}{\mathrm{d}t} = -\frac{1}{3}\alpha^4 g(t) - \frac{\alpha^2}{2}\left[\exp\left(-\frac{\alpha^2 t}{Pe}\right) + \frac{Ma_s}{Ma}q(t)\right], \tag{3.10}$$

$$\frac{\mathrm{d}q(t)}{\mathrm{d}t} = -q(t)\left[\alpha^2\frac{Ma_s}{Ma} + \frac{\alpha^2}{Pe_s}\right] - \frac{\alpha^4}{2}g(t) - \alpha^2\exp\left(-\frac{\alpha^2 t}{Pe}\right), \tag{3.11}$$

which forms a linear system of constant-coefficient inhomogeneous ordinary differential equations. A detailed derivation along with some analytical results are provided in § S.4 of

https://doi.org/10.1017/jfm.2026.11235 Published online by Cambridge University Press

supplementary material. Solutions were obtained numerically using MATLAB's ode15s with initial conditions $g(t) = q(t) = 0$, and are presented under the 'linearised theory' label in subsequent figures.

4. Insoluble surfactant

We first consider an insoluble surfactant initially deposited uniformly at the liquid–air interface with $\Gamma(x, t = 0) = 1$. Similar to prior work (Larsson & Kumar 2021), we solve for the maximum height perturbation Δh, a measure of the maximum deformation that develops, given by

$$\Delta h = \max_t \{\Delta h_t : \Delta h_t = h_{max}(t) - h_{min}(t)\}. \tag{4.1}$$

Here, $h_{max}(t)$ and $h_{min}(t)$ are the maximum and minimum height over the lateral direction x at time t. We also solve for $t_{max} = \operatorname{argmax}_t \Delta h_t$, the time at which Δh occurs.

We stop the simulation once two conditions are met: (i) a maximum height perturbation has been achieved, and (ii) the film has nearly levelled. Condition (i) is satisfied once the height non-uniformity starts decreasing with time. This condition is described by $\Delta h - \Delta h_t > 0$. At early times, the height perturbation grows and this criterion is not yet satisfied. Once a maximum height has been reached, the height deformation levels and $\Delta h_t < \Delta h$. Condition (ii) is met when $\Delta h_t < 10^{-5}$ for an arbitrary time duration, chosen to be ten time steps taken by the solver. In some instances, the film overshoots its levelled state before levelling off due to persistent surfactant Marangoni stresses (see § S.5 of the supplementary material). Ten time steps were sufficient to capture this delevelling phenomenon.

4.1. *Fast-diffusion regime*

We first discuss the regime of relatively low Péclet numbers ($Pe < 10^4$), where solute diffusion is rapid enough to homogenise vertical solute concentration gradients on a much faster time scale relative to other phenomena. The initial perturbation imposed on the solute concentration profile (figure 2*c*) diffuses to the solute-depleted liquid–air interface and causes a laterally inhomogeneous solute composition there. The centre of the film is depleted of solute relative to the edges and will correspond to a high-surface-tension zone (figures 3*a* and 3*c*). Surface-tension gradients set the liquid in motion at the initially flat interface (figure 3*b*), exerting a pull toward the centre of the film. At early times, the surfactant concentration gradients at the interface are relatively weak (figure 3*d*), and this solute Marangoni flow acts mostly uninhibited, easily deforming the film thickness and producing a prominent non-uniformity in the height (figure 3*b*).

Solute Marangoni flow redistributes surfactant so that it is more concentrated at the centre of the film relative to the edges (figure 3*d*). Since surfactant lowers the surface tension, surface-tension gradients arising from solute Marangoni effects are weakened by this surfactant redistribution. In addition, surfactant concentration gradients drive Marangoni stresses that oppose solute Marangoni stresses. Given that solute-driven convection is responsible for the deformation of the initially flat interface, surfactants resist the growth of film-height perturbations.

The competition between solute and surfactant Marangoni flows can be understood through the influence of each species on the change in height as described by (2.9). The two Marangoni contributions in (2.9) are of opposite signs given the opposite direction of their interface concentration gradients. We compare the relative magnitude of each Marangoni flow through the respective solute and surfactant contribution terms, $1/2\ \partial_x[h^2\ \partial_x(\phi|_{z=h})]$

https://doi.org/10.1017/jfm.2026.11235 Published online by Cambridge University Press

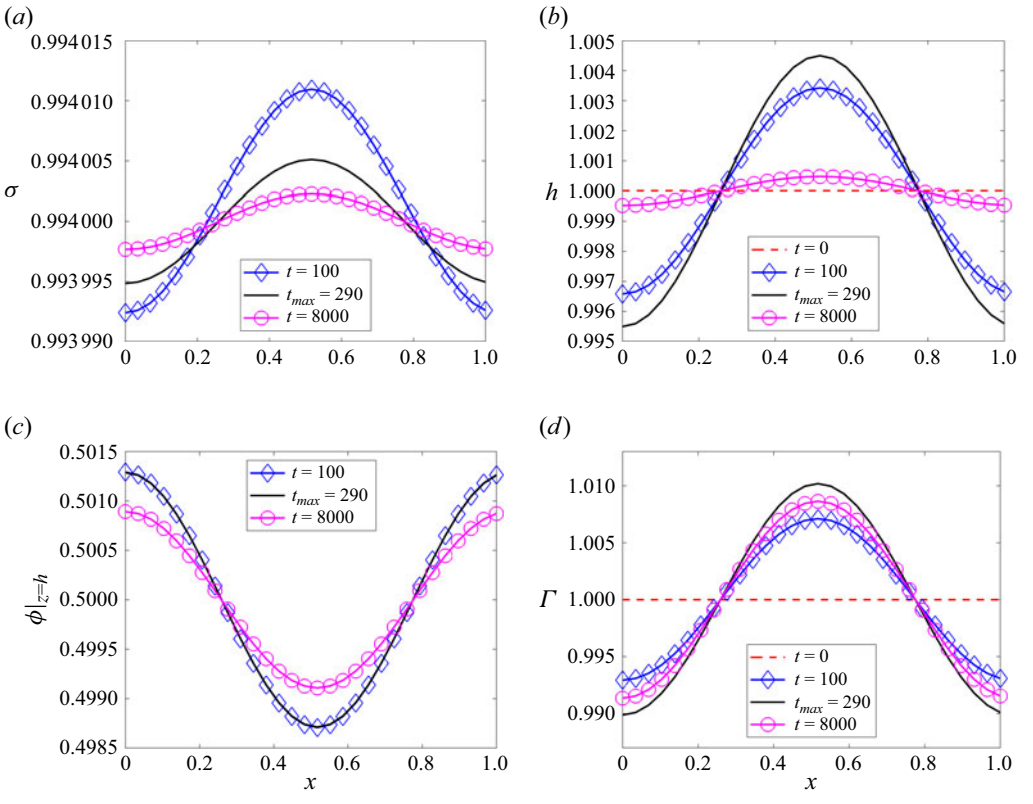


Figure 3. Profiles of (*a*) surface tension σ, (*b*) height h, (*c*) interface solute concentration $\phi|_{z=h}$ and (*d*) interface surfactant concentration Γ for the insoluble case at various times. Here, $Ma = 0.01$, $Pe = 5 \times 10^3$, $Pe_s = 10^3$ and $Ma_s = 0.001$. The surface tension and the interface solute concentration at $t = 0$ are horizontal lines at 0.999 and 0, respectively, and were left out of (*a*) and (*c*) for clarity.

and $1/2(Ma_s/Ma)\partial_x[h^2\partial_x\Gamma]$, where $\partial_x = \partial/\partial x$. We compute the maximum gradient in absolute value over all x-coordinate nodes for each time t using a fourth-order centred finite-difference scheme and plot the result versus time for different Ma_s in figure 4. As Ma_s increases, the maximum solute contribution decreases at any given time while the surfactant contribution increases.

Figure 5(*a*) shows the resulting monotonic decrease in Δh, the maximum amplitude of the interface deformation, with increasing Ma_s. This behaviour is consistent with the suppression mechanisms just described. From figure 5(*c*), we observe that surfactant decreases t_{max}, the time at which the maximum perturbation is reached. At low Ma_s, increasing Pe leads to larger height deformations Δh and higher t_{max}. This is because the lateral solute diffusive time scale increases with Pe and sustains solute concentration gradients at the interface for a longer time. This effect exacerbates solute Marangoni stresses and delays the erasure of solute concentration gradients by lateral diffusion, producing larger Δh and leading to higher t_{max}. The film's behaviour at high Ma_s, which appears independent of Pe, is discussed through a scaling argument in § 4.1.2.

4.1.1. *Accuracy of simplified models*

Figures 5(*b*) and 5(*d*) compare predictions of the two simplified models developed in § 3 with the two-dimensional (2-D) model. The simplified models agree with the 2-D

https://doi.org/10.1017/jfm.2026.11235 Published online by Cambridge University Press

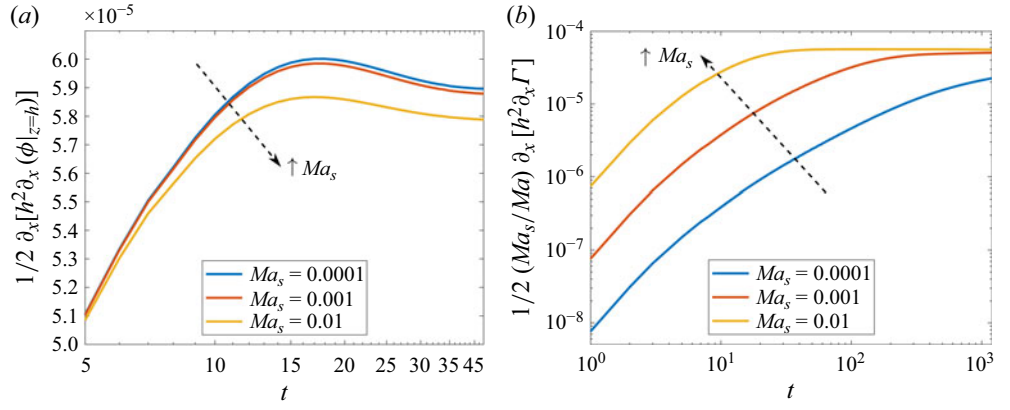


Figure 4. Time evolution of (*a*) solute and (*b*) surfactant contributions to the change in height (second and third terms in (2.9)) for various Ma_s with $Ma = 0.01$, $Pe = 5 \times 10^3$ and $Pe_s = 10^3$.

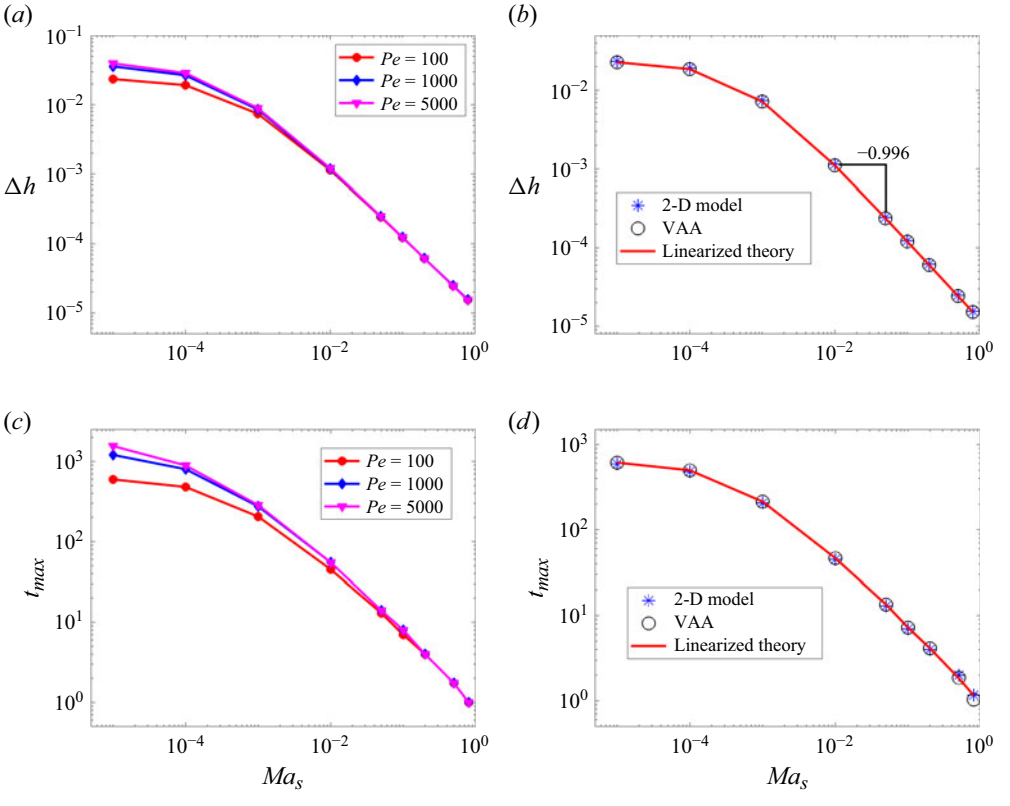


Figure 5. Variation of (*a*) Δh and (*c*) t_{max} with Ma_s for various Péclet numbers in the regime of fast solute diffusion. Comparison of (*b*) Δh and (*d*) t_{max} between the linearised theory, VAA and 2-D model for $Pe = 100$. The other parameters are fixed at $Ma = 0.01$ and $Pe_s = 10^4$. Note that the range $0.1 < Ma_s < 0.9$ was investigated to gain insight into asymptotic behaviour at very high surfactant mass fractions.

https://doi.org/10.1017/jfm.2026.11235 Published online by Cambridge University Press

model for $Pe = 100$ (shown), and to within 10 % for larger values of $Pe < 10^4$ (not shown). At first glance, this result is surprising given the assumption $\epsilon^2 Pe \ll 1$ in the derivation of the VAA, and the additional assumption of dominant lateral solute diffusion over convective effects for the linearised theory. The latter assumption requires $Pe \ll 1$. The observed accuracy up to $Pe = 10^4$ suggests that the height non-uniformity can be accurately predicted while neglecting both the vertical stratification of the solute and convective terms. We note that the maximum deformation values are relatively small due to the relatively small amplitude of the initial concentration perturbation ($\phi_p = 0.01$; see § 2.5). Larger initial perturbations lead to larger height deformations, but also larger concentration gradients in both the vertical and horizontal directions. These gradients are computationally challenging to accurately resolve, so they are not investigated here.

In the fast-diffusion regime, vertical solute concentration gradients are erased rapidly enough so that the two-layer structure behaves as one layer. Vertical solute concentration gradients are homogenised on a time scale of $\epsilon^2 Pe < 100$ for $\epsilon = 0.1$ and $Pe < 10^4$, which is much faster than $t_{max} \geqslant 600$ at low Ma_s (figure 5*d*). Since $\epsilon^2 Pe \ll t_{max}$, the simplified models exploit the disparity between the vertical-diffusion time scale and the time needed to achieve the maximum height deformation by treating the stratified system as a single layer. The VAA employs a 1-D expansion of variables in Fourier modes starting from a vertically uniform initial solute concentration profile, but can achieve comparable accuracy to the 2-D model in this regime of fast solute diffusion. This significantly reduces the computational expense of resolving a vertical solute stratification, which requires a high-order Chebyshev polynomial expansion to accurately describe the solute concentration profile in the vertical direction.

The *Pe* cutoff value of 10^4 matches the previously reported value for the surfactant-free case (Larsson & Kumar 2021), which suggests surfactant presence does not shift this threshold. This makes sense given that the accuracy threshold is largely determined by vertical diffusion of solute from the solute-rich bottom layer to the solute-depleted interface. This diffusion mechanism is controlled by *Pe* (Larsson & Kumar 2021) and is not significantly affected by the surfactant, which is confined to the interface in the insoluble case. As a result, the accuracy threshold defined for the simplified models is insensitive to surfactant redistribution and Ma_s, and is instead primarily controlled by *Pe*.

4.1.2. *Asymptotic behaviour at high Ma_s*

From figures 5(*a*) and 5(*b*), we note $\Delta h \sim Ma_s^{-1}$ when $Ma_s > 0.01$. This is consistent with the asymptotic behaviour of the function $g(t)$ in (3.10), which describes the time dependence of the height perturbation in the linearised theory. It is straightforward to show that in the limit $b = Ma_s/Ma \gg 1$ (see § S.4 of supplementary material for details)

$$\Delta h \sim b^{-1}. \tag{4.2}$$

The regime where the linear slope is observed in figure 5(*a*) corresponds to $b \geqslant 1$. Scaling relation (4.2) reflects the fact that stronger surfactant Marangoni stresses at increasing Ma_s (larger b) lead to smaller height non-uniformities (smaller $g(t_{max})$ and thus smaller Δh) that are more rapidly attained (smaller t_{max}, figures 5*c* and 5*d*).

Figure 5(*a*) also shows nearly overlapping Δh plots at high Ma_s as *Pe* varies over two orders of magnitude. Scaling relation (S.73) in the supplementary material suggests that Δh is relatively insensitive to *Pe* in the fast-diffusion regime when $b \gg 1$, since

$$\Delta h \sim \exp\left(-t_{max}\frac{\alpha^2}{Pe}\right). \tag{4.3}$$

https://doi.org/10.1017/jfm.2026.11235 Published online by Cambridge University Press

The argument of the exponential in (4.3) is responsible for the influence of Pe on Δh. For typical values $\alpha = 0.3$, $t_{max} \leqslant 1000$ and $100 \leqslant Pe \leqslant 10^4$, we obtain $t_{max}\alpha^2/Pe \leqslant 0.9$. In contrast, the effect of surfactant Marangoni stresses on Δh is given by (S.74) of supplementary material as

$$\Delta h \sim \exp\left(-b\alpha^2 t_{max}\right). \tag{4.4}$$

From figure 5(*a*), we note that surfactants exert a significant influence on Δh when $Ma_s \geqslant 0.001$ ($b \geqslant 0.1$). In this regime, the exponential argument in (4.4) exceeds 9. This value is an order of magnitude larger than the exponential argument responsible for Pe effects ($9/0.9 = 10$). We thus expect that variations in Pe will have negligible influence on the maximum height non-uniformity in this regime compared with Ma_s. We also note that (4.3) quickly approaches 0 as $Pe \to 0$, revealing that Δh is insensitive to Pe relative to other parameters when solute diffusion is sufficiently fast. This reasoning agrees with prior work on films devoid of surfactant (Larsson & Kumar 2021) and generalises the dependence of Δh on Pe to the surfactant-laden case.

Physically, scaling relation (4.3) can be interpreted as follows. In the low-Pe regime, vertical diffusion of solute is rapid. The initial lateral perturbation imposed on the solute and localised at $h_b = 0.5$ will diffuse to the interface on a much faster time scale compared with the time needed for Marangoni flows to develop laterally and drive a height non-uniformity. As a result, one-layer predictions are accurate despite treating vertical diffusion as instantaneous in the asymptotic limit of $Pe \to 0$ and employing a vertically uniform initial condition that ignores the initial solute stratification altogether.

4.2. *Slow-diffusion regime*

4.2.1. *Behaviour of Δh and t_{max}*

Figure 6(*a–d*) shows the behaviour of Δh and t_{max} with respect to Ma_s when $Pe > 10^4$. A monotonic decrease of Δh with increasing Ma_s is observed (figures 6*a* and 6*b*), consistent with trends reported in the low-Pe regime (§ 4.1). In contrast, t_{max} tends to plateau at $Ma_s \geqslant 0.01$ in the high-Pe regime (figures 6*c* and 6*d*).

The behaviour at low Ma_s in the high-Pe regime can be understood from results obtained in previous work where surfactants were absent (corresponding to $Ma_s = 0$) (Larsson & Kumar 2021). In this regime, solute diffusion is slow compared with the low-Pe regime, so vertical concentration gradients remain important for longer time and contribute to the developing height non-uniformity. As a consequence, the values of Δh and t_{max} are more sensitive to the value of Pe at low Ma_s (figures 6*a* and 6*c*) compared with the low-Pe regime (figures 5*a* and 5*c*). Moreover, the values of Δh at low Ma_s are generally larger in the high-Pe regime because weaker solute diffusion exacerbates lateral gradients in the solute concentration at the interface. This effect makes it easier for solute-induced Marangoni stresses to deform the interface as previously reported (Larsson & Kumar 2021). Since the interface is initially solute depleted, weaker diffusion of solute at increasing Pe delays the onset of solute Marangoni stresses, which is reflected in the larger values of t_{max} as Pe increases (figures 6*b* and 6*d*). Additionally, since the interface deforms more as Pe increases, it takes longer to reach its maximum deformation, contributing to larger t_{max} at higher Pe. Note that the t_{max} values at low Ma_s and high Pe can actually be smaller than those in the low-Pe regime due to the convective steepening of lateral solute concentration gradients driven by solute Marangoni stresses (Larsson & Kumar 2021).

As might be expected, predictions of the simplified models, which assume a vertically uniform solute concentration, deviate from the 2-D model predictions at low Ma_s in the high-Pe regime (figures 6*b* and 6*d*), in contrast to the excellent agreement observed in

https://doi.org/10.1017/jfm.2026.11235 Published online by Cambridge University Press

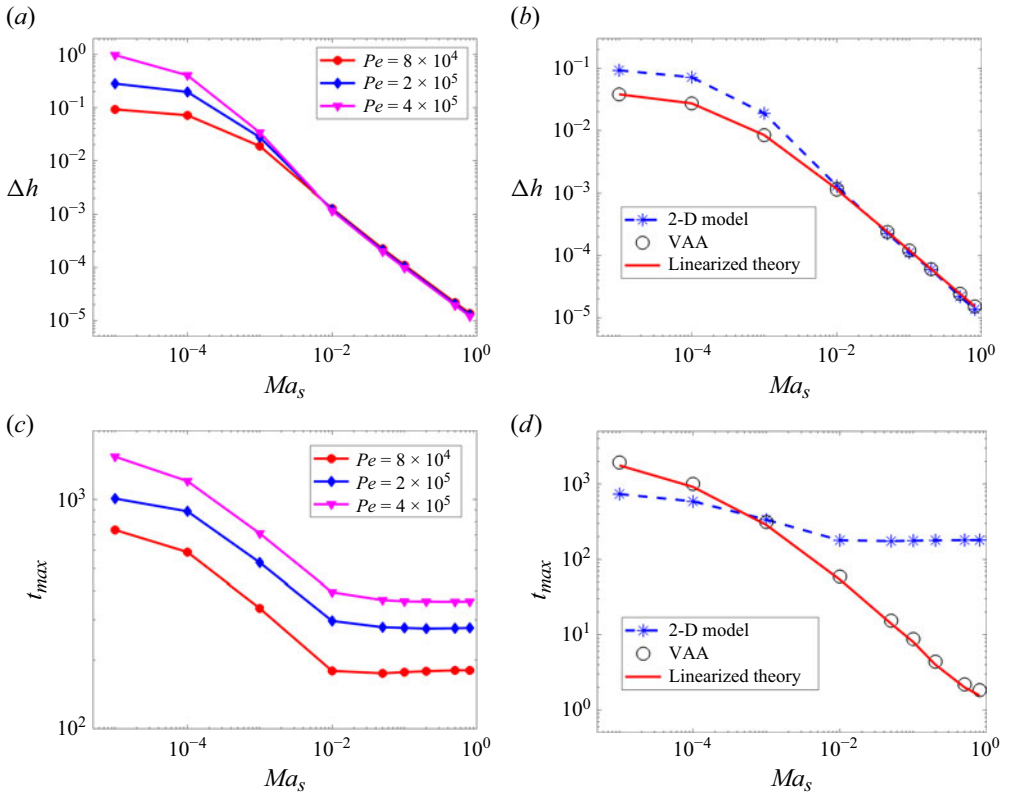


Figure 6. Variation of (*a*) Δh and (*c*) t_{max} with Ma_s for various Péclet numbers in the regime of slow solute diffusion. Comparison of (*b*) Δh and (*d*) t_{max} between the linearised theory, VAA and 2-D model for $Pe = 8 \times 10^4$. The other parameters are fixed at $Pe_s = 10^4$ and $Ma = 0.01$.

the low-*Pe* regime (figures 5*b* and 5*d*). However, the values of Δh become relatively independent of *Pe* at high Ma_s (figure 6*a*) and agree closely with predictions of simplified models in this regime (figure 6*c*). This suggests that sufficiently strong surfactant Marangoni flows can help erase vertical solute concentration gradients and produce a quasi-one-layer structure, as discussed below.

4.2.2. *Marangoni-induced recirculation*

To better understand the high-*Pe* regime, we plot the velocity field and solute concentration contours in figures 7 and 8 for various parameter values. For reference, we first consider the low-*Pe* regime in figure 7. When $t \approx 0.5\, t_{max}$ (figure 7*a*), rapid vertical diffusion has already eliminated steep vertical concentration gradients. The resulting horizontal concentration gradients drive Marangoni flow toward the film centre. When $t \approx 1.5\, t_{max}$ (figure 7*b*), the film has already achieved a maximum height deformation at t_{max} and is in the process of relaxing back to a flat state with flow directed away from the height peak at the film centre. Surfactant has already accumulated at the centre of the film by this time, so surfactant Marangoni flows and capillary levelling act to recover a flat film. The general behaviour shown here is representative of other values of Ma_s, with larger values of Ma_s leading to smaller values of Δh and t_{max}.

We now consider the high-*Pe* regime in figure 8. In figures 8(*a*) and 8(*b*), we observe sharp vertical concentration gradients when $Ma_s = 0$. At the times shown, flow is directed

https://doi.org/10.1017/jfm.2026.11235 Published online by Cambridge University Press

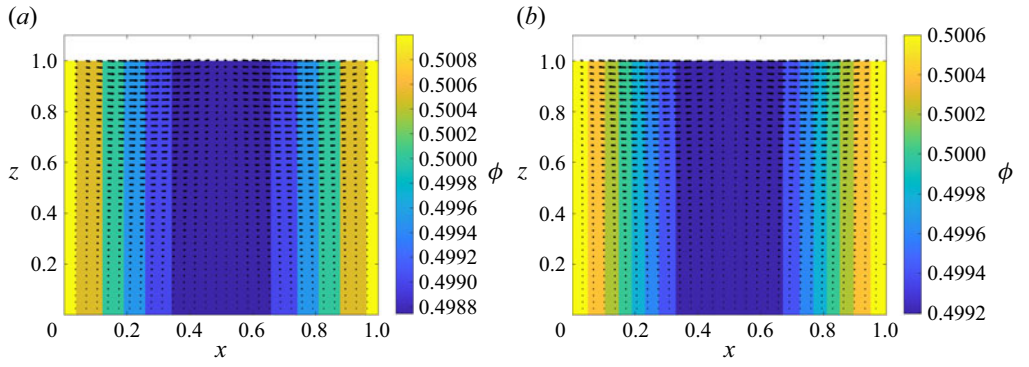


Figure 7. Velocity field plotted over solute concentration contours at (*a*) $t \approx 24 \approx 0.5\, t_{max}$ and (*b*) $t \approx 72 \approx 1.5\, t_{max}$ for $Pe = 10^3$. Other parameters are $Ma = 0.01$, $Ma_s = 0.01$ and $Pe_s = 10^4$. At $t \approx 0.8\, t_{max}$, the velocity field looks very similar to (*a*) and is not shown for brevity.

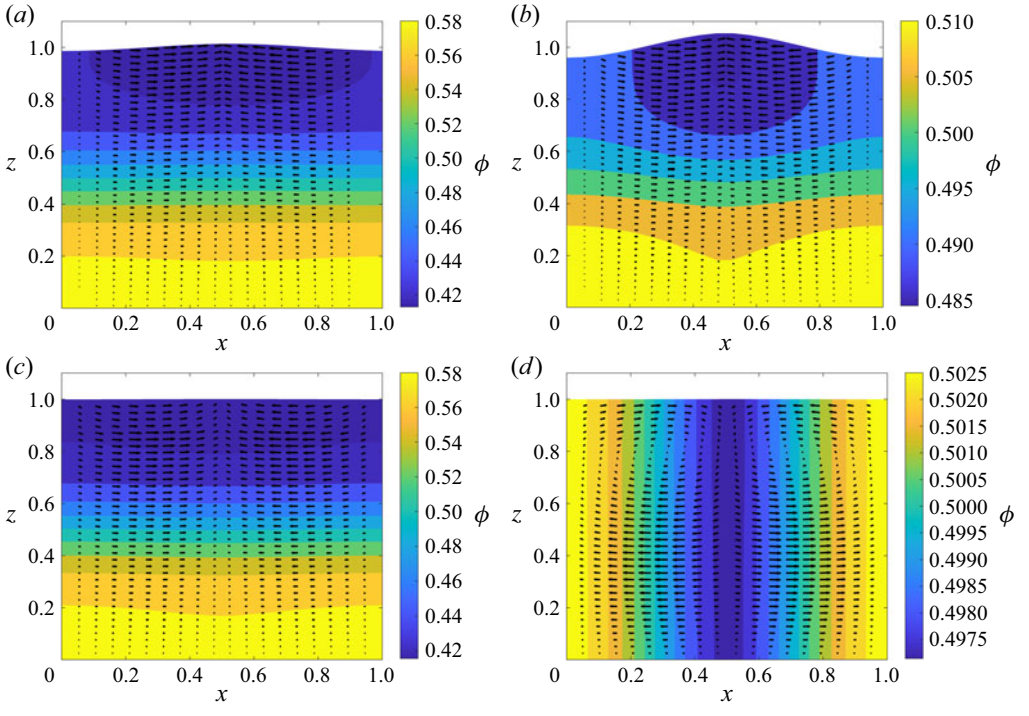


Figure 8. Velocity field plotted over solute concentration contours at $Pe = 10^5$, $Ma = 0.01$ and $Pe_s = 10^4$. Panels show (*a*) $Ma_s = 0$ at $t \approx 374 \approx 0.5\, t_{max}$; (*b*) $Ma_s = 0$ at $t \approx 599 \approx 0.8\, t_{max}$; (*c*) $Ma_s = 0.01$ at $t \approx 101 \approx 0.5\, t_{max}$; (*d*) $Ma_s = 0.01$ at $t \approx 160 \approx 0.8\, t_{max}$.

toward the film centre, similar to the low-*Pe* regime (figure 7*a*) but with a vertically stratified solute concentration. The picture is dramatically different for sufficiently large Ma_s, as seen in figures 8(*c*) and 8(*d*). Although there are significant vertical concentration gradients when $t \approx 0.5\, t_{max}$, those vertical concentration gradients are rapidly smoothed out by the time $t \approx 0.8\, t_{max}$. Additionally, while the flow is directed toward the film centre when $t \approx 0.5\, t_{max}$, a recirculation region is seen when $t \approx 0.8\, t_{max}$. This recirculation mixes the vertically stratified solute and erases its vertical concentration gradients.

https://doi.org/10.1017/jfm.2026.11235 Published online by Cambridge University Press

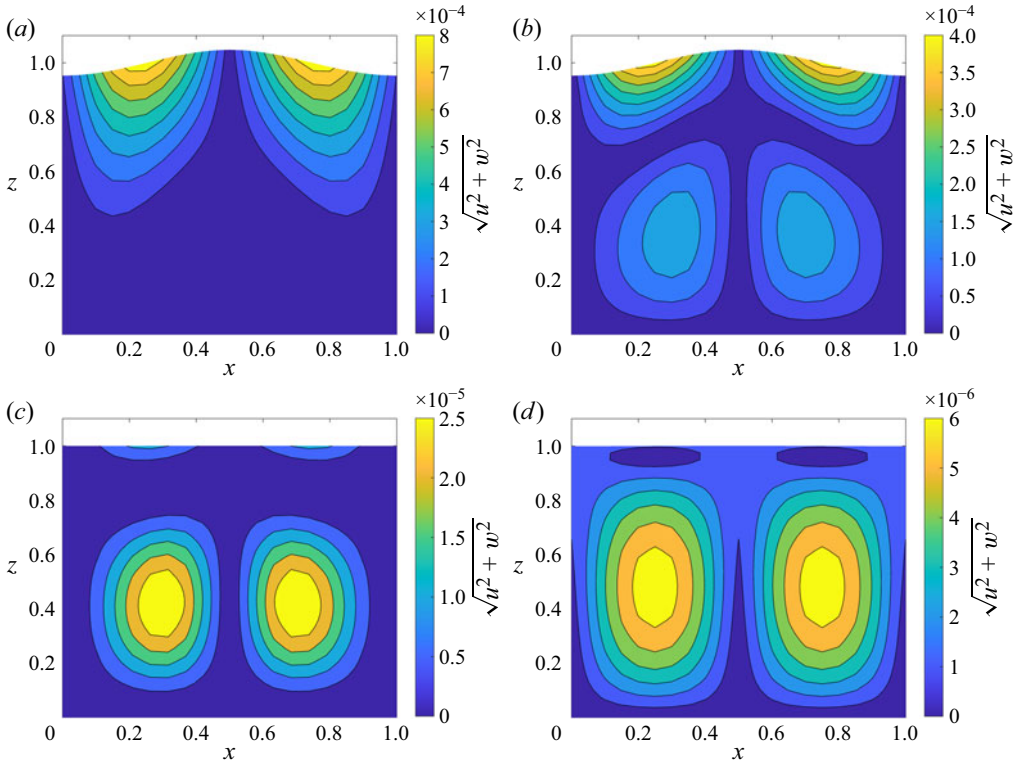


Figure 9. Velocity magnitude contours at $Pe = 10^5$ and $Ma = 0.01$ when (*a*) $Ma_s = 0$ and $t \approx 0.8\, t_{max}$ ($t_{max} \approx 751$), (*b*) $Ma_s = 0$ and $t \approx 0.9\, t_{max}$, (*c*) $Ma_s = 0.01$ and $t \approx 0.8\, t_{max}$ ($t_{max} \approx 200$), (*d*) $Ma_s = 0.01$ and $t \approx 0.9\, t_{max}$.

As a consequence, predictions of Δh at sufficiently high Ma_s approach those obtained from simplified one-layer models (figure 6*b*).

In figures 9(*a*) and 9(*c*), we show velocity magnitude contours corresponding to figures 8(*b*) and 8(*d*). When $Ma_s = 0$, the largest velocities are located at the liquid–air interface for $t < t_{max}$ (figures 9*a* and 9*b*). As t approaches t_{max}, the significant height deformation produced at high Pe results in large capillary stresses that resist further height deformation. Although this is not immediately apparent from figure 9(*b*), recirculation regions are present at $t \approx 0.9\, t_{max}$, similar to what has been previously reported for surfactant-free systems at high Pe for times approaching t_{max} (Larsson & Kumar 2021). However, when $Ma_s = 0.01$, the largest velocities are near the film centre, and flow at the liquid-air interface is nearly stagnant (figures 9*c* and 9*d*). This is due to surfactant-induced Marangoni stresses effectively resisting the solute-induced Marangoni stresses when the value of Ma_s is large, thereby rigidifying the liquid–air interface.

A rigid liquid–air interface corresponds to vanishing tangential motion. In figure 10, we plot the maximum magnitude of the surface-tension gradient over all time and space at low and high Pe. We observe that this maximum, which is proportional to the maximum tangential stress magnitude at the interface, decreases as Ma_s increases, but it does so more rapidly at high Pe. When $Ma_s = 0.01$ and $Pe = 10^5$, the magnitude is very small and is given by $|\partial\sigma/\partial x| \approx 7 \times 10^{-5}$ (figure 10). Since this tangential stress is responsible for liquid flow along the surface but remains negligible at all times $t < t_{max}$, interfacial flows

https://doi.org/10.1017/jfm.2026.11235 Published online by Cambridge University Press

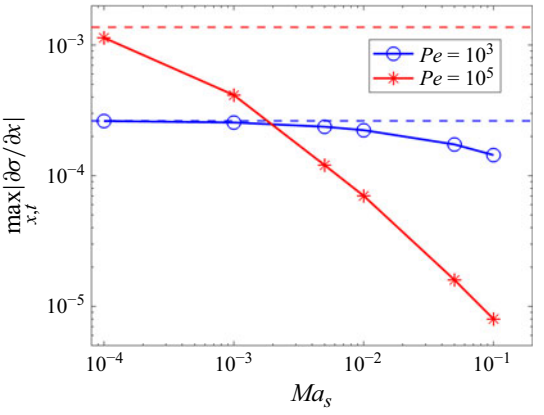


Figure 10. Maximum magnitude of surface-tension gradients at the liquid–air interface over all x and t for various Ma_s at representative values of the low and high-Pe regimes. Here, $Pe_s = 10^4$, $Ma = 0.01$ and dashed lines represent the surfactant-free case ($Ma_s = 0$).

nearly halt. This restriction on interfacial motion at high Pe and high Ma_s prevents further lateral flow at the interface once surfactants have been sufficiently redistributed.

The mechanism for the formation of recirculatory flows at high Pe and high Ma_s can be understood through this rigidification of the interface. At early times, the surfactant concentration at the interface is nearly uniform, and surfactant Marangoni stresses are negligible. This means interfacial velocities develop freely due to solute-driven Marangoni convection. Flow at the free surface propagates into the bulk because a solute-induced Marangoni stress must be balanced by a shear stress in the liquid. When surfactant Marangoni flows become very strong at high Ma_s, a minor surfactant redistribution is sufficient to greatly suppress solute Marangoni stresses, thereby suppressing lateral motion at the interface. While the flow underneath, which is being dragged toward the film centre, is expected to deform the liquid-air interface, it fails to do so when the interface resists motion and is effectively rigid. As a result, lateral flow is redirected downward at the centre of the film and fluid at the edges will flow upward to conserve mass in the liquid film, giving rise to recirculation regions. Surfactants can thus precipitate the formation of recirculation regions at high Pe in films with initial vertical gradients in the solute concentration.

Predictions of t_{max} from simplified models in figure 6(d) exhibit similar behaviour to the low-Pe regime (figure 5d), given that these models ignore vertical concentration gradients and model the system as a one-layer film. In contrast, the 2-D model predicts smaller values of t_{max} at low Ma_s compared with the simplified models because of the convective steepening effect discussed by Larsson & Kumar (2021). This effect is recovered in the limit of $Ma_s \to 0$ where surfactant Marangoni stresses are non-existent. As Ma_s increases, surfactants decrease the maximum height non-uniformity via mechanisms similar to those described in § 4.1 and help achieve t_{max} more rapidly. Note that since the interface becomes effectively rigid at sufficiently high Ma_s, the values of t_{max} reach a plateau at $Ma_s = 0.01$, as seen in figure 6(c). While t_{max} becomes insensitive to Ma_s in this regime, it remains sensitive to Pe. Solute must first reach the interface before a height deformation takes place and before the surfactant gets redistributed by solute Marangoni flows. The rate-limiting step for these processes is the slow vertical diffusion of solute, which is controlled by Pe. Higher Pe values delay interface rigidification and lead to large t_{max} as a result (figure 6c).

We have also examined the influence of the surfactant Péclet number Pe_s on Δh and found its effect to be negligible. A reversal in the height deformation at $t > t_{max}$ can take

https://doi.org/10.1017/jfm.2026.11235 Published online by Cambridge University Press

place when surfactant diffusion is slow relative to solute diffusion (high Pe_s, low Pe) because surfactant concentration gradients at the interface persist and generate Marangoni stresses that overwhelm those of the solute. Further details are provided in § S.5 of the supplementary material.

4.3. *Connection to experimental observations*

Although there are several differences between the model developed in this work and the experiments conducted by Horiuchi *et al.* (2015), including but not limited to their use of two distinct solvents (water and glycerol) for the individual layers and the relatively concentrated SDS solutions they deposited, qualitative comparisons can provide valuable insights into underlying physical mechanisms. They found decreasing film-height non-uniformities at increasing surfactant mass fractions. We have found in this work that increasing Ma_s can significantly improve the uniformity of multilayer coatings by suppressing solute-driven Marangoni flows, which is reflected in smaller Δh at increasing Ma_s observed in our simulations. Since $Ma_s \sim w_{surfactant}$ in our model (table 2), our findings are qualitatively consistent with the observations of Horiuchi *et al.*, The lack of a non-uniformity metric in their experiments renders a quantitative comparison with our model difficult. However, the significant decrease in Δh with increasing Ma_s we have observed suggests that non-uniformities can decrease and cease to induce dewetting through the mechanisms we have delineated when sufficiently high surfactant mass fractions are used.

5. Soluble surfactant

We now discuss the effects of surfactant solubility. Motivated by the experiments of Horiuchi *et al.* (2015), we consider a soluble surfactant concentrated in the top layer using initial condition (2.23). At $t = 0$, the bottom layer is surfactant depleted, while the interface is at a surfactant-exchange equilibrium with the surfactant-rich top layer.

5.1. *Effects of Bi and β*

Surfactant solubility is characterised by two parameters that we vary here: Bi and β. The Biot number $Bi = k^H_{des} L/U$ measures the strength of surfactant desorption relative to convection. The solubility coefficient $\beta = k^H_{ads}/(k^H_{des} H)$ measures the strength of surfactant adsorption relative to desorption.

Figure 11(a) shows the sensitivity of the maximum height deformation Δh to Bi. In the limit of low Bi, Δh approaches a plateau close to its predicted value for insoluble surfactants. Surfactant desorption is weak in this regime because $Bi \sim k^H_{des}$. As a result, surfactant concentration gradients can develop at the interface and produce strong surfactant Marangoni stresses. As Bi increases, faster surfactant desorption weakens the associated Marangoni stresses, leading to an increase in Δh. For high values of Bi, Δh approaches a plateau close to the value for the no-surfactant case.

Note that the plateaus seen in figure 11(a) are offset from the limiting cases shown by the dashed lines. The exchange flux J is small at low values of Bi but is not negligible. For $\beta = 1$ and $Pe_b = 10^4$, the contribution $(c|_{z=h} - \Gamma)$ in (2.17) grows with time, causing loss of surfactant mass from the interface into the bulk. This effect decreases the amount of surfactant available at the interface over time and weakens surfactant Marangoni effects compared with the insoluble case, leading to the offset as $Bi \to 0$ (figure 11a). The variation of Δh with respect to Bi in figure 11(a) is observed for a wide range of β and Pe_b values, with offsets from the asymptotic limits $Bi \to 0$ and $Bi \to \infty$ that

https://doi.org/10.1017/jfm.2026.11235 Published online by Cambridge University Press

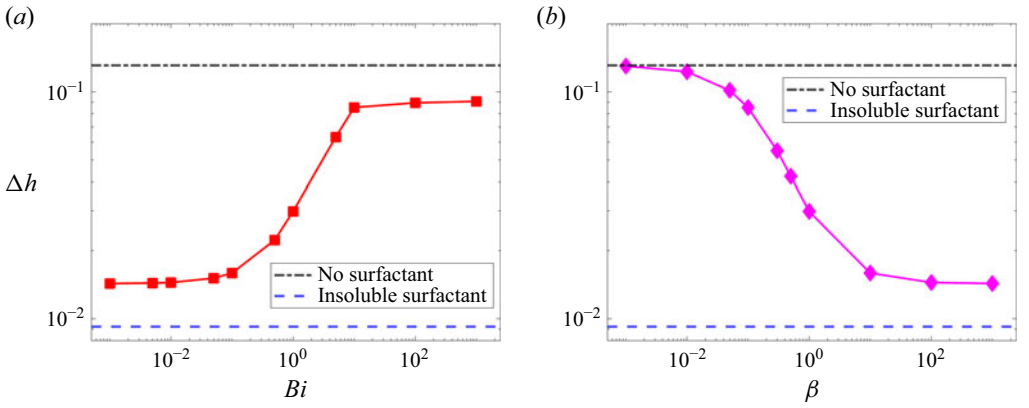


Figure 11. Solubility effects measured through variations in Δh as a function of (*a*) Bi and (*b*) β. We fix $\beta = 1$ in (*a*) and $Bi = 1$ in (*b*). Remaining parameter values are $Ma = 0.01$, $Ma_s = 2 \times 10^{-3}$, $Pe_b = Pe_s = 10^4$ and $Pe = 1.5 \times 10^5$.

depend on surfactant solubility (β) and the bulk surfactant diffusion time scale (Pe_b). When $\beta \geqslant 100$ and $Bi \leqslant 0.01$ (not shown), the height non-uniformity is within 2 % of the insoluble-surfactant case so that the offset from the insoluble limit is smaller than in figure 11(*a*).

At $Bi = 1$, surfactant Marangoni effects are strong enough to suppress the height deformation by nearly an order of magnitude (figure 11*a*). We fix $Bi = 1$ in figure 11(*b*), and vary β to better understand the role of surfactant solubility on the growth of the height non-uniformity. In the limit of low surfactant solubility (high β), surfactants exhibit high affinity for the interface and strongly suppress Δh due to a reduction in the associated Marangoni stresses. The value of Δh approaches a plateau close to the value for insoluble surfactants. Note that because $Bi = 1$ in these calculations, there is still significant surfactant desorption relative to convection, so the plateau is offset from the insoluble-surfactant value. As β decreases, the surfactant becomes more soluble in the liquid bulk, which weakens surfactant Marangoni stresses and increases Δh. In the limit of high surfactant solubility (low β), the height non-uniformity approaches the surfactant-free limit.

5.2. *Effect of Pe_b*

To investigate the effect of surfactant diffusion in the liquid bulk on the height non-uniformity, we vary Pe_b. Figure 12(*a*) shows that Δh decreases as the diffusion of surfactant in the bulk slows down (increasing Pe_b). Slower bulk diffusion strengthens surfactant Marangoni stresses and leads to greater height suppression. We note that the calculations become increasingly stiff as $Pe_b \to 0$ (due to fast surfactant diffusion) and $Pe_b \to \infty$ (due to steep concentration gradients). However, results from calculations we have performed for other parameter regimes (not shown here) indicate that Δh should reach plateaus as $Pe_b \to 0$ and $Pe_b \to \infty$. These plateaus may be offset from the limiting cases shown by the dashed lines in figure 12 depending on the values of Bi and β (see § 5.1).

To better understand the impact of Pe_b on surfactant-induced surface-tension gradients, we plot in figure 12(*b*) the subsurface concentration of surfactant $c(x, z = h, t)$ over time at the centre of the film. At high Pe_b (10^5), surfactant diffusion within the liquid bulk is relatively slow, so it can maintain a high surfactant concentration at the subsurface. Slow vertical diffusion of surfactant in the film will aim to replenish the surfactant-depleted

https://doi.org/10.1017/jfm.2026.11235 Published online by Cambridge University Press

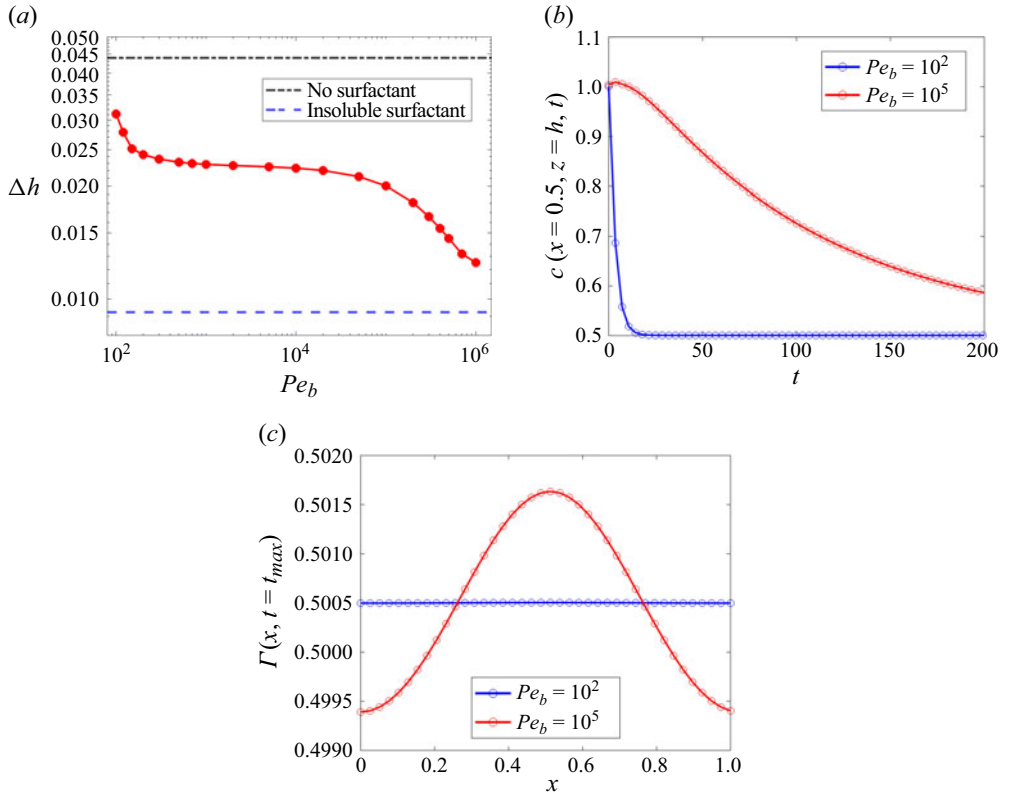


Figure 12. (*a*) Variation of Δh with Pe_b for soluble surfactant. (*b*) Variation of the subsurface surfactant concentration (at $z = h$) with time at fixed $x = 0.5$ (centre of the film). (*c*) Surfactant concentration at the interface at t_{max}. All other parameters in (*a–c*) are fixed at $Ma = 0.01$, $Pe = Pe_s = 10^4$, $\beta = 1$, $Bi = 0.01$ and $Ma_s = 0.001$.

bottom layer but will fail to rapidly deplete the initially surfactant-rich top layer at high Pe_b. As a consequence, the subsurface region remains sufficiently enriched in surfactant so that it can sustain a high surfactant concentration at the interface through the rapid surfactant-exchange equilibrium. As surfactant accumulates at the centre of the interface due to solute Marangoni flows, it remains concentrated there for extended time and develops substantial lateral concentration gradients. Surfactants become more effective at suppressing surface-tension gradients that arise from the solute and can better counteract solute Marangoni flows when Pe_b is large, which helps achieve smaller Δh (figure 12*a*).

In contrast, figure 12(*b*) shows the subsurface is rapidly depleted of surfactant at lower Pe_b (10^2). The fast diffusion of surfactant in the liquid bulk strips surfactant away from the interface and produces a depletion region at the subsurface. Figure 12(*b*) shows that $c(x = 0.5, z = h, t)$ sharply drops and remains at a vertically averaged concentration of $c \approx 0.5$ in the low-Pe_b regime. Surfactant in the liquid diffuses to the surfactant-depleted bottom layer because of vertical concentration gradients imposed by the initial stratification of the surfactant. The surfactant-rich regions of the interface that develop over time will experience rapid surfactant desorption into the depletion zone to re-establish the surfactant-exchange equilibrium with the subsurface (since $c(x, z = h, t) \approx 0.5 < 1$). As a result, lateral gradients in the surfactant concentration at the interface are rapidly erased as they form and fail to become substantial. Figure 12(*c*) reflects this through the contrast

https://doi.org/10.1017/jfm.2026.11235 Published online by Cambridge University Press

between the nearly uniform surfactant concentration at the interface at t_{max} for sufficiently small Pe_b and the prominent lateral gradients that exist at sufficiently large Pe_b.

6. Conclusion

We presented and analysed mechanisms for surfactant suppression of film-thickness perturbations in multicomponent two-layer coatings using a model based on lubrication theory. Initial perturbations to the solute concentration field can vertically diffuse to the interface, generate surface-tension gradients and drive flows that deform the film thickness. Surfactants get redistributed by such flows and compete with the solute to resist height deformations via surfactant-driven Marangoni stresses. This finding is qualitatively consistent with the flow visualisation experiments of Horiuchi *et al.* (2015).

We have shown that surfactant effectiveness in controlling height perturbations is primarily governed in the low-*Pe* regime by the surfactant Marangoni number Ma_s, which characterises the sensitivity of surface tension to surfactant concentration gradients at the interface. High Ma_s values are desirable for surfactant Marangoni convection to effectively counteract solute Marangoni flows. We evaluated the performance of two approximations that hinge on fast diffusion of the solute: a VAA and a linearised theory. These simplified models accurately predict the height non-uniformity in the presence of surfactants at low *Pe* but fail to do so when $Pe > 10^4$ and $Ma_s \ll 1$. At sufficiently large Ma_s in the high-*Pe* regime, the interface becomes rigid (i.e. the tangential velocity vanishes) and strongly resists deformation. Surfactants precipitate the formation of recirculation zones in the film, which smooth out vertical gradients in the solute concentration and improve the agreement between the predictions of the simplified and 2-D models.

Our model further reveals that surfactant solubility in the bulk weakens its suppression mechanisms and can significantly influence the height deformation. For sufficiently small Pe_b values, rapid diffusion of surfactant in the liquid bulk depletes the subsurface region of surfactant and favours further desorption from the interface. This diffusion mechanism hinders the growth of surfactant Marangoni flows. In contrast, slow surfactant diffusion in the bulk at high Pe_b preserves a surfactant-rich subsurface for longer time while the fast surfactant adsorption–desorption equilibrium sustains steep surfactant concentration gradients at the interface. The resulting surfactant Marangoni stresses are highly effective at resisting the height deformation.

In practical applications, it is often desired to have a vertically stratified solute concentration profile to impart desirable functionalities to the final coating (see § 1). In addition, a smooth coating is typically desired. Our results show that while the addition of surfactants can lead to a smoother coating, it can also destroy the vertical stratification of the solute, even under conditions where the solute Péclet number is large (see § 4.2). A better understanding of the impacts of this tradeoff will require consideration of solvent evaporation, which is an essential step for obtaining a solidified coating. Evaporation will tend to cause solute buildup at the liquid–air interface, which may exacerbate solute-driven Marangoni flows, but will also raise the viscosity of the coating, which will make it harder to deform the interface. The model developed here can readily be extended to account for these effects, as well as others, such as the influence of higher surfactant concentrations via a nonlinear equation of state for surface tension.

Supplementary material. Supplementary material is available at https://doi.org/.10.1017/jfm.2026.11235

Acknowledgements. This work was supported by the Industrial Partnership for Research in Interfacial and Materials Engineering of the University of Minnesota. We also acknowledge partial support through the PPG Foundation (via a fellowship to R. B.), and through the donors of ACS Petroleum Research Fund under

https://doi.org/10.1017/jfm.2026.11235 Published online by Cambridge University Press

ACS-PRF 66930-ND9. We are grateful to the Minnesota Supercomputing Institute (MSI) at the University of Minnesota for its high-performance computational resources. We thank C. Larsson for helpful discussions.

Declaration of interests. The authors report no conflicts of interest.

References

ALKINDI, A.S., AL-WAHAIBI, Y.M. & MUGGERIDGE, A.H. 2008 Physical properties (density, excess molar volume, viscosity, surface tension, and refractive index) of ethanol + glycerol. *J. Chem. Engng Data* **53** (12), 2793–2796.

BARHOUM, S. & YETHIRAJ, A. 2010 An NMR study of macromolecular aggregation in a model polymer-surfactant solution. *J. Chem. Phys.* **132** (2), 024909.

BENOUAGUEF, I., MUSUNURI, N., AMAH, E.C., BLACKMORE, D., FISCHER, I.S. & SINGH, P. 2021 Solutocapillary Marangoni flow induced in a waterbody by a solute source. *J. Fluid Mech.* **922**, A23.

BOYD, J.P. 2001 *Chebyshev and Fourier Spectral Methods: Second Revised Edition*. Courier Corporation.

CHANG, C.-H. & FRANSES, E.I. 1995 Adsorption dynamics of surfactants at the air/water interface: a critical review of mathematical models, data, and mechanisms. *Colloids Surf. A Physicochem. Engng Aspects* **100**, 1–45.

CHEN, Q., DRISCOLL, T.A. & BRAUN, R.J. 2024 Evaporation-driven tear film thinning and breakup in two space dimensions. *J. Engng Maths* **149** (1), 5.

DEY, M., VIVEK, A.S., DIXIT, H.N., RICHHARIYA, A. & FENG, J.J. 2019 A model of tear-film breakup with continuous mucin concentration and viscosity profiles. *J. Fluid Mech.* **858**, 352–376.

ECCHER, J., ZAJACZKOWSKI, W., FARIA, G.C., BOCK, H., VON SEGGERN, H., PISULA, W. & BECHTOLD, I.H. 2015 Thermal evaporation versus spin-coating: electrical performance in columnar liquid crystal OLEDs. *ACS Appl. Mater. Interfaces* **7** (30), 16374–16381.

EDMONSTONE, B.D., CRASTER, R.V. & MATAR, O.K. 2006 Surfactant-induced fingering phenomena beyond the critical micelle concentration. *J. Fluid Mech.* **564**, 105–138.

ERES, M.H., WEIDNER, D.E. & SCHWARTZ, L.W. 1999 Three-dimensional direct numerical simulation of surface-tension-gradient effects on the leveling of an evaporating multicomponent fluid. *Langmuir* **15** (5), 1859–1871.

HENDERSON, D.C. & MICALE, F.J. 1993 Dynamic surface tension measurement with the drop mass technique. *J. Colloid Interface Sci.* **158** (2), 289–294.

HORIUCHI, R., SUSZYNSKI, W.J. & CARVALHO, M.S. 2015 Simultaneous multilayer coating of water-based and alcohol-based solutions. *J. Coatings Technol. Res.* **12**, 819–826.

IWE, I.A., GOSTEVA, E.A., STARKOV, V.V., SEDLOVETS, D.M. & MONG, O. 2019 Anti-glare coatings based on porous silicon structures. *ES Mater. Manufacturing* **3** (3), 47–51.

JENSEN, O.E. & GROTBERG, J.B. 1993 The spreading of heat or soluble surfactant along a thin liquid film. *Phys. Fluids A: Fluid Dyn.* **5** (1), 58–68.

KAHLWEIT, M., STREY, R. & BUSSE, G. 1991 Effect of alcohols on the phase behavior of microemulsions. *J. Phys. Chem.* **95** (13), 5344–5352.

KALOGIROU, A. & BLYTH, M.G. 2020 Nonlinear dynamics of two-layer channel flow with soluble surfactant below or above the critical micelle concentration. *J. Fluid Mech.* **900**, A7.

KALPATHY, S.K., FRANCIS, L.F. & KUMAR, S. 2012 Thin-film models of liquid displacement on chemically patterned surfaces for lithographic printing processes. *J. Colloid Interface Sci.* **383** (1), 155–166.

KÖLLNER, T., SCHWARZENBERGER, K., ECKERT, K. & BOECK, T. 2013 Multiscale structures in solutal Marangoni convection: three-dimensional simulations and supporting experiments. *Phys. Fluids* **25** (9), 092109.

LARSSON, C. & KUMAR, S. 2021 Nonuniformities in miscible two-layer two-component thin liquid films. *Phys. Rev. Fluids* **6** (3), 034004.

LARSSON, C. & KUMAR, S. 2022 Quantitative analysis of the vertical-averaging approximation for evaporating thin liquid films. *Phys. Rev. Fluids* **7** (9), 094002.

MATAR, O.K. 2002 Nonlinear evolution of thin free viscous films in the presence of soluble surfactant. *Phys. Fluids* **14** (12), 4216–4234.

MOORE, M.R., VELLA, D. & OLIVER, J.M. 2021 The nascent coffee ring: how solute diffusion counters advection. *J. Fluid Mech.* **920**, A54.

MORGAN, C.E., BREWARD, C.J.W., GRIFFITHS, I.M., HOWELL, P.D., PENFOLD, J., THOMAS, R.K., TUCKER, I., PETKOV, J.T. & WEBSTER, J.R.P. 2012 Kinetics of surfactant desorption at an air–solution interface. *Langmuir* **28** (50), 17339–17348.

NG, G.-M., KIETZKE, E.L., KIETZKE, T., TAN, L.-W., LIEW, P.-K. & ZHU, F. 2007 Optical enhancement in semitransparent polymer photovoltaic cells. *Appl. Phys. Lett.* **90** (10), 103505.

https://doi.org/10.1017/jfm.2026.11235 Published online by Cambridge University Press

ORON, A., DAVIS, S.H. & BANKOFF, S.G. 1997 Long-scale evolution of thin liquid films. *Rev. Mod. Phys.* **69** (3), 931.

PARK, N.-G. & ZHU, K. 2020 Scalable fabrication and coating methods for perovskite solar cells and solar modules. *Nat. Rev. Mater.* **5** (5), 333–350.

PEREIRA, A. & KALLIADASIS, S. 2008 On the transport equation for an interfacial quantity. *Eur. Phys. J. Appl. Phys.* **44** (2), 211–214.

PHAM, T., CHENG, X. & KUMAR, S. 2017 Drying of multicomponent thin films on substrates with topography. *J. Polym. Sci. B: Polym. Phys.* **55** (22), 1681–1691.

PHAM, T. & KUMAR, S. 2019 Imbibition and evaporation of droplets of colloidal suspensions on permeable substrates. *Phys. Rev. Fluids* **4** (3), 034004.

PHAN, C.M., NGUYEN, A.V. & EVANS, G.M. 2005 Dynamic adsorption of sodium dodecylbenzene sulphonate and dowfroth 250 onto the air–water interface. *Miner. Engng* **18** (6), 599–603.

PRATT, K.C. & WAKEHAM, W.A. 1974 The mutual diffusion coefficient of ethanol–water mixtures: determination by a rapid, new method. *Proc. R. Soc. Lond. A Math. Phys. Sci.* **336** (1606), 393–406.

PROSSER, A.J. & FRANSES, E.I. 2001 Adsorption and surface tension of ionic surfactants at the air–water interface: review and evaluation of equilibrium models. *Colloids Surf. A: Physicochem. Engng Aspects* **178** (1–3), 1–40.

RODRÍGUEZ-HAKIM, M., BARAKAT, J.M., SHI, X., SHAQFEH, E.S.G. & FULLER, G.G. 2019 Evaporation-driven solutocapillary flow of thin liquid films over curved substrates. *Phys. Rev. Fluids* **4** (3), 034002.

SAMANTA, A. 2025 Effect of soluble surfactant on thermocapillary instability in falling film. *Phys. Rev. Fluids* **10** (6), 064001.

SCHULZ, M. & KEDDIE, J.L. 2018 A critical and quantitative review of the stratification of particles during the drying of colloidal films. *Soft Matt.* **14** (30), 6181–6197.

SERPETSI, S.K. & YIANTSIOS, S.G. 2012 Stability characteristics of solutocapillary Marangoni motion in evaporating thin films. *Phys. Fluids* **24** (12), 122104.

TODOROV, T. & MITZI, D.B. 2010 Direct liquid coating of chalcopyrite light-absorbing layers for photovoltaic devices. *Eur. J. Inorganic Chem.* **2010** (1), 17–28.

TREFETHEN, L.N. 1996 Finite difference and spectral methods for ordinary and partial differential equations. Unpublished text. Available at: https://people.maths.ox.ac.uk/trefethen/pdetext.html.

VAZQUEZ, G., ALVAREZ, E. & NAVAZA, J.M. 1995 Surface tension of alcohol water+ water from 20 to 50°C. *J. Chem. Engng Data* **40** (3), 611–614.

WEINHEIMER, R.M., EVANS, D.F. & CUSSLER, E.L. 1981 Diffusion in surfactant solutions. *J. Colloid Interface Sci.* **80** (2), 357–368.

WILL, J., MITTERDORFER, A., KLEINLOGEL, C., PEREDNIS, D. & GAUCKLER, L.J. 2000 Fabrication of thin electrolytes for second-generation solid oxide fuel cells. *Solid State Ionics* **131** (1–2), 79–96.

WILSON, S.K. 1993 The levelling of paint films. *IMA J. Appl. Maths* **50** (2), 149–166.

WOOLFREY, S.G., BANZON, G.M. & GROVES, M.J. 1986 The effect of sodium chloride on the dynamic surface tension of sodium dodecyl sulfate solutions. *J. Colloid Interface Sci.* **112** (2), 583–587.

YIANTSIOS, S.G., SERPETSI, S.K., DOUMENC, F. & GUERRIER, B. 2015 Surface deformation and film corrugation during drying of polymer solutions induced by Marangoni phenomena. *Intl J. Heat Mass Transfer* **89**, 1083–1094.

https://doi.org/10.1017/jfm.2026.11235 Published online by Cambridge University Press